

---

# RANDOMIZED PRIOR WAVELET NEURAL OPERATOR FOR UNCERTAINTY QUANTIFICATION

---

A PREPRINT

**Shailesh Garg**

Department of Applied Mechanics  
Indian Institute of Technology Delhi  
Hauz Khas, New Delhi 110016, India.  
shaileshgarg96@gmail.com

**Souvik Chakraborty**

Department of Applied Mechanics  
Yardi School of Artificial Intelligence (YScAI)  
Indian Institute of Technology Delhi  
Hauz Khas, New Delhi 110016, India.  
souvik@am.iitd.ac.in

February 3, 2023

## ABSTRACT

In this paper, we propose a novel data-driven operator learning framework referred to as the *Randomized Prior Wavelet Neural Operator* (RP-WNO). The proposed RP-WNO is an extension of the recently proposed wavelet neural operator, which boasts excellent generalizing capabilities but cannot estimate the uncertainty associated with its predictions. RP-WNO, unlike the vanilla WNO, comes with inherent uncertainty quantification module and hence, is expected to be extremely useful for scientists and engineers alike. RP-WNO utilize randomized prior networks, which can account for prior information and is easier to implement for large, complex deep-learning architectures than its Bayesian counterpart. Four examples have been solved to test the proposed framework, and the results produced advocate favorably for the efficacy of the proposed framework.

**Keywords** Uncertainty Quantification · Wavelet Neural Operator · Randomized Prior Networks · Neural Networks

## 1 Introduction

Uncertainty is an inextricable part of any dataset originating from a physical process. The physical process under consideration can be natural, like weather phenomena [1, 2], or artificial, like building deflections [3–5]. These uncertainties [6, 7] can manifest themselves in the form of (i) aleatoric uncertainty or (ii) epistemic uncertainty, or both. Aleatoric uncertainty is primarily present due to the inherent randomness in the physical process. Measurement noise can also be a potential source of aleatoric uncertainty in datasets collected using the internet of things. Since the sources of aleatoric uncertainty are ineradicable, it is often termed irreducible uncertainty. The other form of uncertainty that may be present is epistemic uncertainty, which originates from incomplete knowledge about the physical process under consideration. Since, theoretically, one can increase their understanding of a physical process by collecting sufficient data, epistemic uncertainty is also termed reducible uncertainty. Even though theoretically, the epistemic uncertainty is reducible given sufficient data, practically, it can never be entirely eliminated due to constraints like limited storage capacity and limited data collection time.

Now, while working with any physical process, knowing the associated uncertainty in various forms can lend the user auxiliary confidence, especially in decision-making tasks. Knowing aleatoric uncertainty can inform the user about the deviation of the system from a mean state, and knowing the epistemic uncertainty tells the user about the adequacy of the dataset chosen for decision-making. Let us now momentarily focus on the problem of generating datasets for any physical process. Due to physical constraints (like time and field storage capacity) and scientific constraints (like sensor technology or placement issues), the real-life data available for various physical processes is limited. Thus it falls upon the user to augment this data with artificial data to increase the total quantum. To generate this artificial data, we need to develop suitable computationally efficient algorithms that can learn the mapping between a physical system’s observed inputs and outputs. Furthermore, in applications like reliability analysis [8–10] or design

optimization [11–13], where repeated simulations are needed, these algorithms can be used as a surrogate model to reduce the computational cost associated with detailed analysis.

In the available literature, techniques like polynomial chaos expansion [14–16], response surface method [17–21], and Gaussian process [22–25] have been used to develop surrogate models in the past, but in recent times, researchers have started to explore heavily deep learning-based techniques. Deep learning [26, 27] algorithms have gained traction in a wide array of fields [28–36] owing to their enormous capacity for modification, low prediction cost, and flexibility in implementation. Learning the mapping between inputs and outputs of a physical process can now be achieved by deep learning based data-driven operator learning algorithms. Recently proposed Wavelet Neural Operator [37, 38] (WNO), DeepONet [9, 39, 40], and Fourier Neural Operator [41] are among the popular operator learning algorithms which have shown tremendous generalization capacity despite being data-driven algorithms. Function approximation algorithms like Physics Informed Neural Networks [42], which utilize the system’s governing equation directly, may also be used. However, these are limited in their applications as complete knowledge of physics is required to converge successfully to the solution. Such limitations are not placed on data-driven algorithms.

Theoretically, estimating aleatoric uncertainty is trivial given a sufficiently large dataset, which is feasible using an appropriate surrogate model. However, estimating epistemic uncertainty is nontrivial and requires algorithms specifically designed for the same. In deep learning, uncertainty quantification can be achieved using either Bayesian or frequentist approaches. The former utilizes Bayesian inference [43] for uncertainty quantification. Among Bayesian methods, Monte Carlo based approaches [44, 45] are the most accurate, but they are impractical in the face of complex deep neural network architectures. Another popular Bayesian approach is to utilize variational inference [46, 47] based methods. These, although can be implemented for complex neural architectures, give only an approximate solution and may fail to converge altogether for multi-modal posterior distributions. Frequentist approaches, on the other hand, are generally easier to implement owing to them being set in a deterministic framework. In frequentist approaches, ensemble training [48] is among the most popular way to estimate uncertainty. However, in vanilla ensemble training, there is no mechanism to include prior information.

In this paper, we introduce a novel Randomized Prior Wavelet Neural Operator (RP-WNO). The proposed RP-WNO utilizes the concepts of random prior networks [49] and enables estimation of epistemic uncertainty (predictive uncertainty) associated with its predictions; this allows users to take well-informed decisions. The capacity of randomized prior networks to incorporate prior information while being set in a frequentist domain makes them a prime candidate for the proposed framework. Four examples have been covered in the paper showcasing the efficacy of the proposed algorithm in both maintaining the generalization capacity of WNO and enabling uncertainty quantification, which was previously not possible within the WNO architecture.

The rest of the paper is arranged as follows. Section 2 discusses the WNO and introduces the proposed RP-WNO. Section 3 discusses various examples showcasing the efficacy of the proposed framework, and section 4 concludes the manuscript.

## 2 Proposed framework

An operator is a mathematical entity that transforms an  $\mathcal{I}$  dimensional input function space to a  $\mathcal{O}$  dimensional output function space. The relation can be described as,

$$f_{\mathcal{I}} \in \mathbb{R}^{\mathcal{I}} \xrightarrow{\mathbb{O}} f_{\mathcal{O}} \in \mathbb{R}^{\mathcal{O}}, \quad (1)$$

where  $\mathbb{O}$  denotes the operator, mapping the input functions to the output functions. In deep learning based operator learning schemes, the goal is to learn the operator by learning the mapping between the two function spaces. In WNO, wavelet transform is leveraged along with CNNs to learn the mapping and, by extension, the operator  $\mathbb{O}$ .

### 2.1 Wavelet neural operator

WNO, proposed in [37], is a deep learning based operator learning scheme that utilizes wavelet blocks within its architecture to achieve its target. The effectiveness of any deep learning based scheme is heavily affected by the quality of data it receives for training. Data with concise and dense information is easier to learn when compared with data having a lot of noise and redundant information. This is simply explained by the fact that to learn a dense dataset, fewer weights and biases will be required, which makes the backpropagation easier and more precise. To this end, in WNO, wavelet transform is used, which extracts the relevant information from the input data while reducing the dimensionality, thus making it easier to learn the mapping between inputs and outputs.

WNO takes  $n$  input functions along with the grid on which they are discretized as its inputs and lifts them to a higher dimension using a densely connected layer. For a two-dimensional domain, discretized using a grid having  $r$  rows,  $c$

columns, and  $s$  samples, the above transaction in terms of dataset dimension evolution can be visualized as,

$$\mathbf{I} \in \mathbb{R}^{s \times r \times c \times n+2} \xrightarrow{\text{Dense layer}} \mathbf{O}_D \in \mathbb{R}^{s \times r \times c \times p}, \quad (2)$$

where  $\mathbf{I}$  is the input to WNO and  $\mathbf{O}_D$  is the output from the densely connected layer having  $p$  nodes. Note that  $p > n + 2$  and in the absence of grid information for the input function, the input dimension will change from  $(s \times r \times c \times n + 2)$  to  $(s \times r \times c \times n)$ . The output from the densely connected block is passed onto the wavelet block, and its dimensions are preserved after the final operations of the wavelet block.

### 2.1.1 Wavelet block

In the WNO architecture, once the input is uplifted, it is passed onto wavelet blocks (WB) which are structured in such a way that they can extract relevant information from the data while keeping the parameter requirement of the neural network low. This is achieved by using wavelet transform and convolutional neural networks. WBs have two main components, (i) Wavelet Mapping Component (WMC) and (ii) Convolution Mapping Component (CMC). Both the components accept the same input and, after processing, return outputs with the same dimensions as input.

Wavelet Transform (WT) used in WMC divides the data into high-frequency and low-frequency wavelet coefficients and downsizes the data, extracting the relevant information. WMC first performs multi-level WT of the input. Through this, we can (i) distill only the relevant information while reducing the overall dimension and (ii) reduce the number of parameters required for learning features from the data. Upon satisfactory dimension reduction, the wavelet coefficients obtained after the final level of wavelet transform can be learned using simple dense linear layers. Now, using the output from the linear layers, inverse wavelet transform is performed. It should be noted that after the final level of the wavelet transform, either all or only the selected wavelet coefficients can be learned using the dense linear layers. The coefficients that are not learned are used as is while inverse wavelet transform.

The WT performed within the WMC can be continuous or discrete depending on the requirement of the dataset being learned. Continuous wavelet transform is more precise than the discrete wavelet transform, and it produces more wavelet coefficients that can be learned for better performance; however, it is computationally more expensive as compared to the discrete wavelet transform. The evolution of dataset size for the previous example of a two-dimensional dataset inside WMC, considering Discrete WT (DWT), can be tracked as follows,

$$\begin{aligned} \mathbf{I}_{WB} \in \mathbb{R}^{s \times r \times c \times p} \xrightarrow{\text{WT}} \mathbf{O}_{WT} \in \mathbb{R}^{s \times r' \times c' \times p \times 4} \xrightarrow{\text{Dense linear layer}} \\ \mathbf{O}_{DLL} \in \mathbb{R}^{s \times r' \times c' \times p \times 4} \xrightarrow{\text{Inverse WT}} \mathbf{O}_{WMC} \in \mathbb{R}^{s \times r \times c \times p}, \end{aligned} \quad (3)$$

where  $\mathbf{I}_{WB}$  is the input for the WB and  $\mathbf{I}_{WB} = \mathbf{O}_D$  for the first wavelet block inside WNO architecture.  $\mathbf{O}_{WT}$  is output after performing multiple WTs.  $r' < r$  and  $s' < s$  are the reduced dimensions of the data after multi-level DWT, and since DWT will give four wavelet coefficients for the two-dimensional domain, the same is reflected in the dataset size.  $\mathbf{O}_{DLL}$  is the output from the dense linear layer, which preserves its input size, and  $\mathbf{O}_{WMC}$  is the final output obtained after the inverse wavelet transform. It should be noted that the dimension for the  $\mathbf{O}_{WMC}$  is the same as that of the  $\mathbf{I}_{WMC}$ .

Next, inside CMC, convolution layers are used in such a way that the final output size is preserved. For the two-dimensional space, the evolution of dataset size inside CMC can be tracked as follows,

$$\mathbf{I}_{WB} \in \mathbb{R}^{s \times r \times c \times p} \xrightarrow{\text{Convolution layers}} \mathbf{O}_{CMC} \in \mathbb{R}^{s \times r \times c \times p}, \quad (4)$$

where  $\mathbf{O}_{CMC}$  is the final output from the CMC. The outputs from the two components of WB are added in order to obtain the final output  $\mathbf{O}_{WB} = \mathbf{O}_{WMC} + \mathbf{O}_{CMC}$ . For second and subsequent WBs inside the WNO architecture,  $\mathbf{I}_{WB}$  is equal to  $\mathbf{O}_{WB}$  from the previous WB. A schematic for the information flow inside WB is shown in Fig. 1 After obtaining the output  $\mathbf{O}_{WB}$ , from the final wavelet block, densely connected layers are used in order to reduce the dimension of the uplifted data so that it may match the final output size. For the two-dimensional space, if the mapping is carried out for a single output function, the evolution of dataset size after the final wavelet block can be tracked as,

$$\mathbf{O}_{FWB} \in \mathbb{R}^{s \times r \times c \times p} \xrightarrow{\text{Forward neural net}} \mathbf{O}_{WNO} \in \mathbb{R}^{s \times r \times c \times 1}, \quad (5)$$

where  $\mathbf{O}_{FWB}$  is output of the final WB and  $\mathbf{O}_{WNO}$  is the final output from the WNO. A schematic for the WNO architecture is shown in Fig. 2. For more details regarding WNO architecture, the readers are referred to [37].

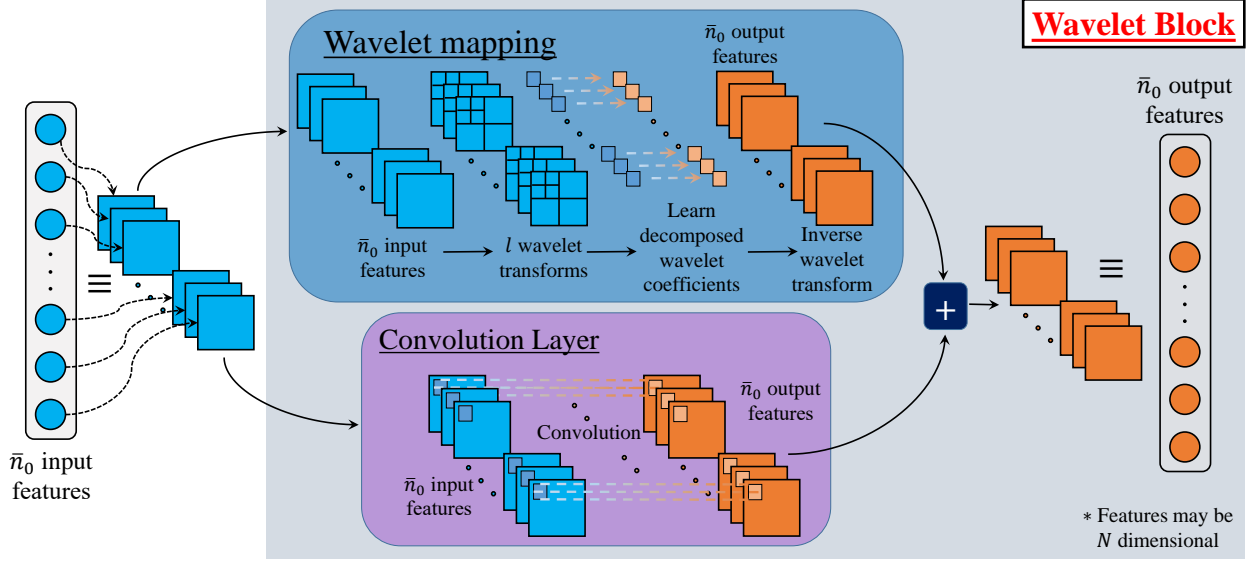


Figure 1: Schematic for information flow inside WBs.

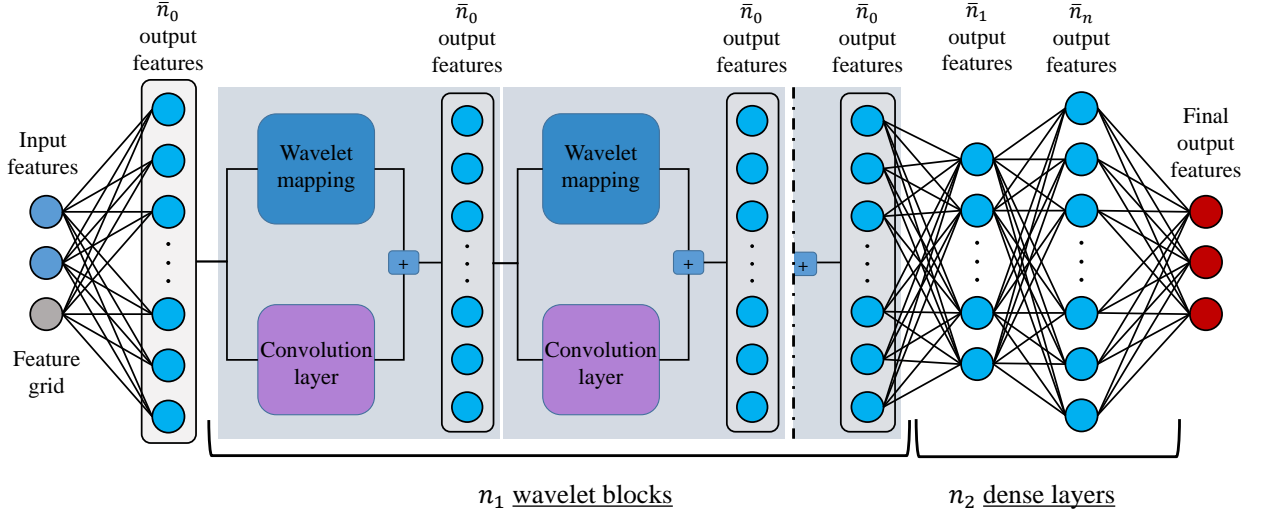


Figure 2: Schematic for the wavelet neural operator.

## 2.2 Randomized Prior WNO (RP-WNO)

The proposed RP-WNO utilizes Randomized Prior (RP) networks introduced in [49] for uncertainty quantification. RP networks utilize two neural networks with identical architectures but different random initialization to enable uncertainty quantification in deep learning models. Among the two networks, one has trainable weights and biases (trainable network), and the other has fixed weights and biases (non-trainable network). Similar to ensemble training, multiple copies of the randomized prior network are trained for uncertainty quantification. The advantage here is that the network with fixed weights and biases makes it possible to incorporate prior information, which was previously not possible in the vanilla ensemble training. Now, during training, in each forward pass, the output from the trainable and non-trainable networks are added before back-propagating for the trainable network. The output  $\mathbf{O}_{RP}$  of a RP network can be described as,

$$\mathbf{O}_{RP} = \mathbf{O}_T + \beta \mathbf{O}_{NT}, \quad (6)$$

where  $\mathbf{O}_T$  is the output of the trainable network and  $\mathbf{O}_{NT}$  is the output for the non-trainable network. It should be noted that the loss function for the RP network is computed based on output obtained from Eq. (6), and while back-

propagating, the weights and biases of only the trainable network are updated.  $\beta$  in Eq. (6) is a hyper-parameter and its value is user defined. In the prevailing literature, it is observed that  $\beta = 1$  produces optimum results.

In the proposed RP-WNO, following the theory of RP networks, two identical WNO networks are taken, one being trainable and the other non-trainable. The outputs for the two are added, and the RP-WNO output  $\mathbf{O}_{RP-WNO}$  is described as follows,

$$\mathbf{O}_{RP-WNO} = \mathbf{O}_{WNOT} + \mathbf{O}_{WNONT}, \quad (7)$$

where  $\mathbf{O}_{WNOT}$  is the output from the trainable WNO model and  $\mathbf{O}_{WNONT}$  is the output from the non-trainable WNO model. A  $\beta$  value of unity is selected following the prevailing literature and the  $\beta$  studies carried out in A. A schematic for the proposed RP-WNO is shown in Fig. 3. To enable uncertainty quantification, we need to train multiple copies of

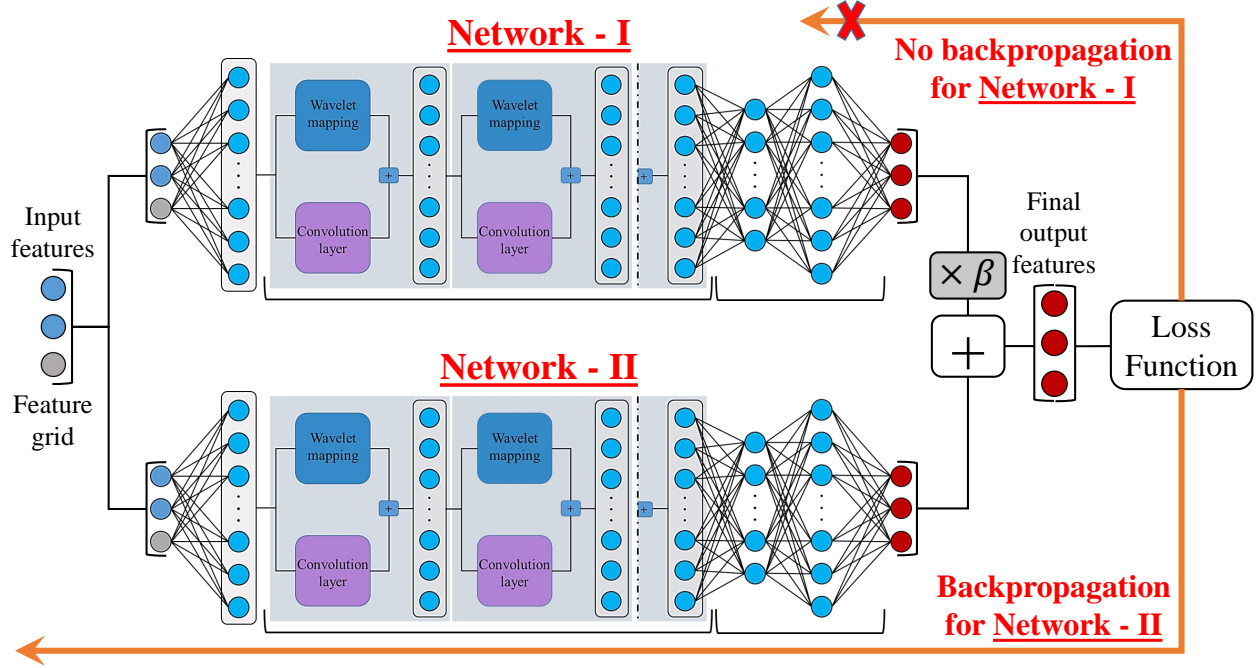


Figure 3: Schematic of the proposed RP-WNO.

RP-WNO, each with different initialization but the same architecture and training data. Since training any two copies of RP-WNO has no bearing on each other, we may train them in parallel, thus saving the overall computational time. Assuming  $\mathcal{P}_i$  is the prediction from the  $i^{\text{th}}$  copy of RP-WNO, the mean prediction  $\mathcal{P}_M$  can be obtained as,

$$\mathcal{P}_m = \frac{1}{n_c} \sum_{i=1}^{n_c} \mathcal{P}_i, \quad (8)$$

where  $n_c$  denotes the number of copies of RP-WNO trained for the same input data. The standard deviation  $\mathcal{P}_s$  of the predictions can be obtained as follows,

$$\mathcal{P}_s = \sqrt{\frac{\sum_{i=1}^{n_c} (\mathcal{P}_i - \mathcal{P}_m)^2}{n_c}}. \quad (9)$$

Note that if  $\mathcal{P}_i$  is a vector or a multidimensional array, the operations stipulated in Eqs. (8) and (9) will be implemented as element-wise operations. The 95% confidence intervals can now be computed as  $\mathcal{P}_m \pm 1.96\mathcal{P}_s$ . Algorithm 1 details the steps involved in training the proposed RP-WNO ensemble. It should be noted that the outputs for the non-trainable network corresponding to the training data can be computed after the initialization step and stored for use later while training to save computational time. Additionally, multiple RP-WNO models in the RP-WNO ensemble can be trained simultaneously in parallel, as training for one has no bearing on the other.

---

**Algorithm 1** Training algorithm for the RP-WNO.

---

```

1: for  $i = 1$  : no. of RP-WNO networks in the ensemble do
2:   Initialize weights and bias for the trainable WNO and the non-trainable WNO with the
   same architecture.
3:   for  $j = 1$  : no. of epochs do
4:     for  $k = 1$  : no. of batches do
5:       Input training data to trainable network and obtain  $\mathcal{O}_{WNOT}$ .
6:       Input training data to non-trainable network and obtain  $\mathcal{O}_{WNONOT}$ .
7:       Compute the combined output,  $\mathcal{O}_{RP-WNO} = \mathcal{O}_{WNOT} + \mathcal{O}_{WNONOT}$ .
8:       Compute the relevant loss function using  $\mathcal{O}_{RP-WNO}$ .
9:       Perform backpropagation and update the trainable network's weights and biases.
10:    end for
11:  end for
12:  Save the trained models for prediction later.
13: end for

```

**Output:** Ensemble of trained RP-WNO networks.

---

### 3 Numerical illustrations

This section covers four case studies to illustrate the efficacy of the proposed RP-WNO. The first case study (CS-I) deals with a one-dimensional, time-dependent Burger's equation, while the second case study (CS-II) deals with a two-dimensional Darcy flow equation. The third case study (CS-III) aims to solve the seismic wave equation for variable velocity models, while the fourth case study (CS-IV) aims to link atomic structural defects to mesoscale properties in crystalline solids. The datasets for the first two case studies have been generated using the codes given in paper [37,41]. The velocity fields for the third case study have been pulled from [50]. For the fourth case study, the datasets are pulled from [51]. The RP-WNO ensembles in the first and second case study utilize discrete wavelet transform, while the RP-WNO ensembles in the third and fourth case study utilize continuous wavelet transforms within the RP-WNO architecture. Further details regarding individual case studies are provided in the respective subsections.

#### 3.1 CS-I: Burger's equation

The one-dimensional Burger's equation under consideration has periodic boundary conditions and is defined as,

$$\frac{\partial u(x, t)}{\partial t} + u \frac{\partial u(x, t)}{\partial x} = \nu \frac{\partial^2 u(x, t)}{\partial x^2},$$

$$x \in [0, 1], \quad t \in (0, 1]$$

$$u(x, 0) \sim \mathcal{N}(0, 625(-\Delta + 25 \mathbb{I})^{-2})$$
(10)

where  $\nu$  is the viscosity of the flow being modeled. For the current case study,  $\nu$  is taken equal to 0.01. The initial condition for Burger's equation is sampled from a Gaussian random field as shown in Eq. (10), where  $\Delta$  is a Laplacian operator. The mapping between the initial condition  $u(x, 0)$  and the velocity field obtained at  $t = 1$ ,  $u(x, 1)$  is learned using the proposed RP-WNO. Fig. 4 shows the mean prediction and confidence intervals obtained using the RP-WNO

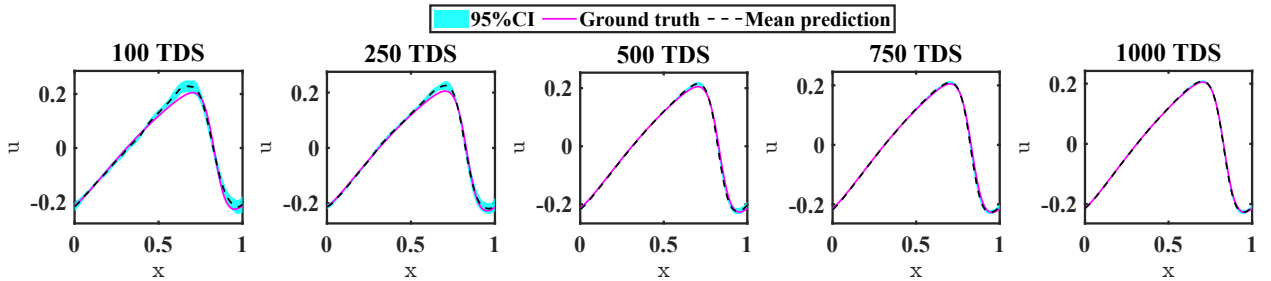


Figure 4: RP-WNO predictions when trained for different numbers of Training Data Samples (TDS) in CS-I.

corresponding to a varying number of Training Data Samples (TDS). It is observed that the uncertainty associated with the prediction decrease as the data available for training increase, which is the expected behavior. Additionally,

Table 1: MAE and mean Std. of RP-WNO predictions in CS-I.

Training samples	100	250	500	750	1000
MAE	0.0192	0.0098	0.0046	0.0033	0.0025
Mean Std.	0.0107	0.0072	0.0039	0.0031	0.0027

the mean prediction converges to the ground truth with an increase in TDS. Table 1 quantifies the results shown in Fig. 4. To generate the Mean Absolute Error (MAE) and mean Standard deviation (Std.), a prediction ensemble with 8000 samples was generated using the trained RP-WNO ensemble. To calculate MAE values, mean predictions from RP-WNO were compared against the ground truth, and for mean Std. values, the variation observed within the RP-WNO ensemble was considered. As can be seen that the trend observed in Table 1, further solidifies the observations associated with Fig. 4.

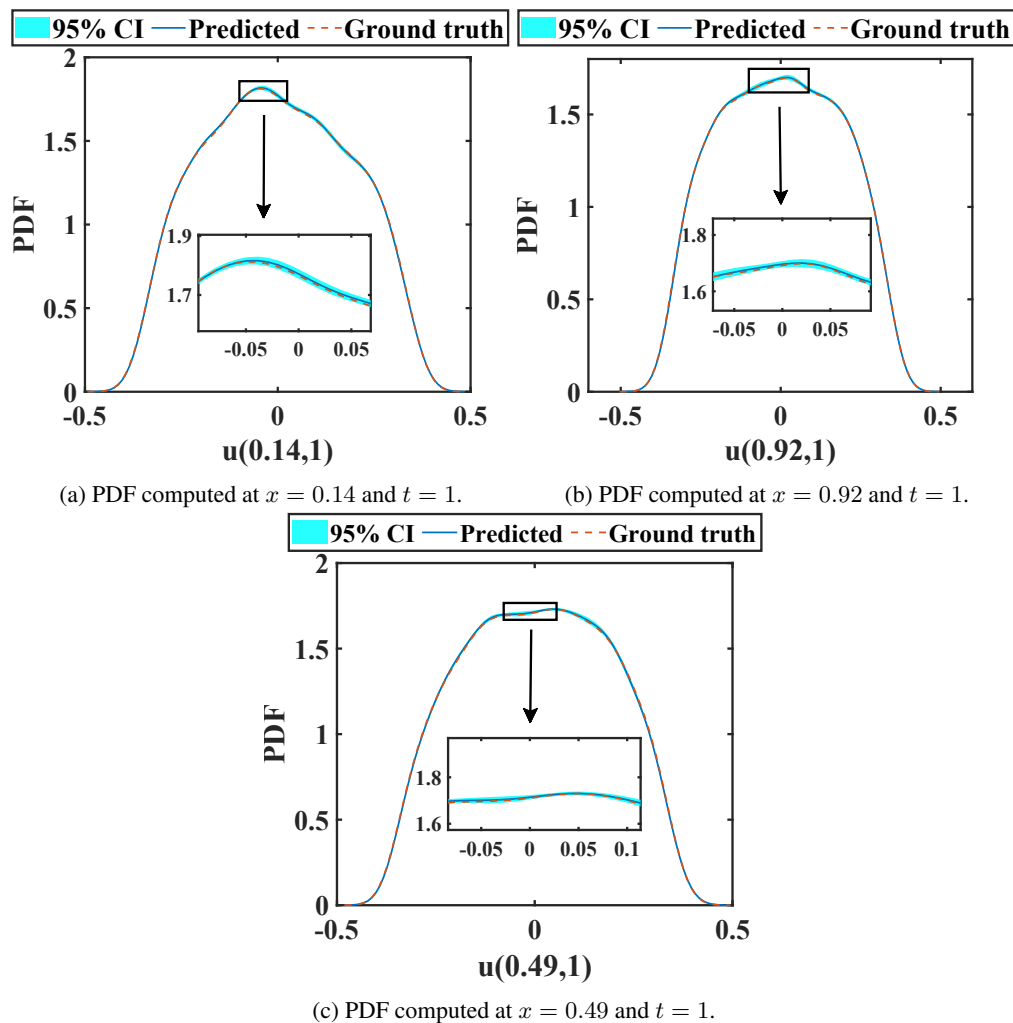


Figure 5: Alleatoric uncertainty estimates for CS-I.

Fig. 5 shows the aleatoric uncertainty estimates compared against the ground truth for the case when the RP-WNO model is trained for 1000 training samples. RP-WNO predictions closely follow the ground truth and provide additional confidence intervals that effectively capture the ground truth.

### 3.2 CS-II: Darcy flow equation

The time-independent two-dimensional Darcy flow equation is given as,

$$\begin{aligned} -\nabla(a(x, y)\nabla u(x, y)) &= 1, \\ x \in (0, 1), \quad y \in (0, 1), \\ a(x, y) &\sim \psi\mathcal{N}(0, (-\Delta + 9\mathbb{I})^{-2}), \end{aligned} \quad (11)$$

where  $a(x, y)$  is the permeability field and is sampled from the Gaussian random field  $\mathcal{N}(0, (-\Delta + 9\mathbb{I})^{-2})$ .  $\Delta$  in Eq. (11) is Laplacian with zero Neumann boundary condition, and  $\psi$  is a mapping that transforms the function such that the positive values are set to 12 and the negative values to 3. Mapping for this case study is carried out between the permeability field  $a(x, y)$  and the corresponding pressure  $u(x, y)$ . Similar to the previous case study, Fig. 6 shows the

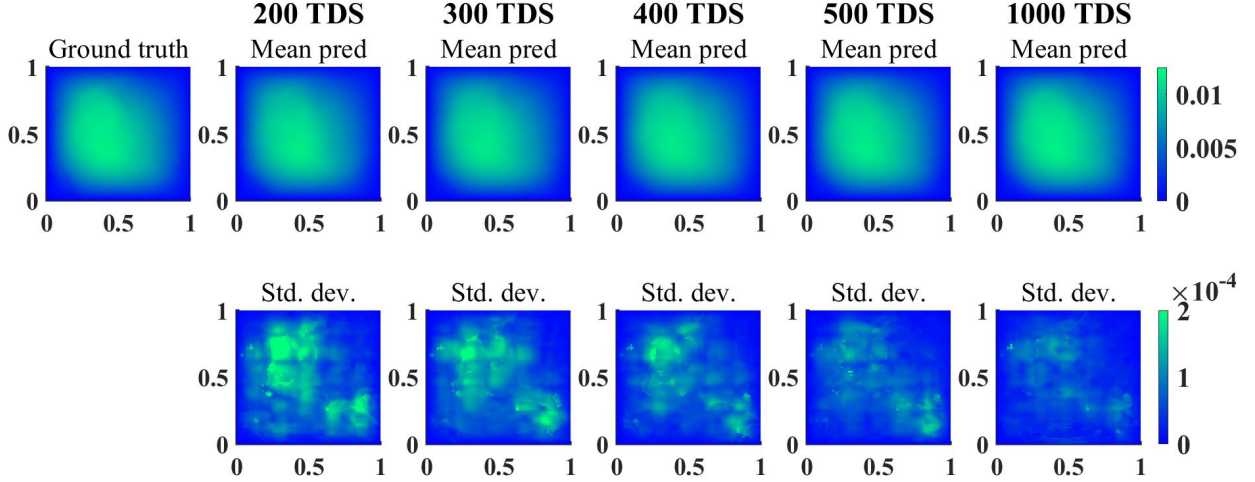


Figure 6: RP-WNO predictions when trained for different numbers of Training Data Samples (TDS) in CS-II.

prediction results for the two-dimensional Darcy flow case study when the RP-WNO ensemble is trained for different numbers of training samples. The results follow the expected trend, and the variation observed in prediction reduces with an increase in the training data. The trend for the evolution of MAE and mean Std. with the increase in training

Table 2: MAE and mean Std. of RP-WNO predictions in CS-II.

Training samples	200	300	400	500	1000
MAE ( $\times 10^{-3}$ )	0.1280	0.0962	0.0770	0.0631	0.0408
Mean Std. ( $\times 10^{-4}$ )	0.7224	0.6025	0.5323	0.4813	0.3601

data is shown in Table 2. Eight thousand test samples were used to arrive at the presented results. Both MAE and mean Std. decrease monotonically, which was the expected behavior.

Fig. 7 shows the aleatoric uncertainty estimates for the two-dimensional Darcy flow equation in CS-II. As can be seen, the mean prediction closely follows the ground truth, and we also obtain additional confidence intervals associated with the proposed RP-WNO predictions. This clearly illustrates the proposed RP-WNO can capture such multimodal distributions. The RP-WNO ensemble was trained using 1000 training samples to obtain the results.

### 3.3 CS-III: Helmholtz equation

For the third case study, we will consider the Helmholtz equation, the solution for which gives pressure wavefields in the frequency domain. Its use case can be found in applications where the effect of traveling waves has to be studied, for example, in electromagnetic radiation studies, seismic ground exploration, etc. The Helmholtz equation for waves traveling in two dimensions is defined as,

$$\nabla^2 u(x, z; w) + k^2 u(x, z; w) = f(x_s, z_s; w), \quad (12)$$

where  $u$  is the pressure wavefield in the frequency domain, and  $w$  is the angular frequency.  $k$  is the wave number, and the point source is located at the location  $(x_s, z_s)$ . In the current case study, for dataset generation, the Helmholtz



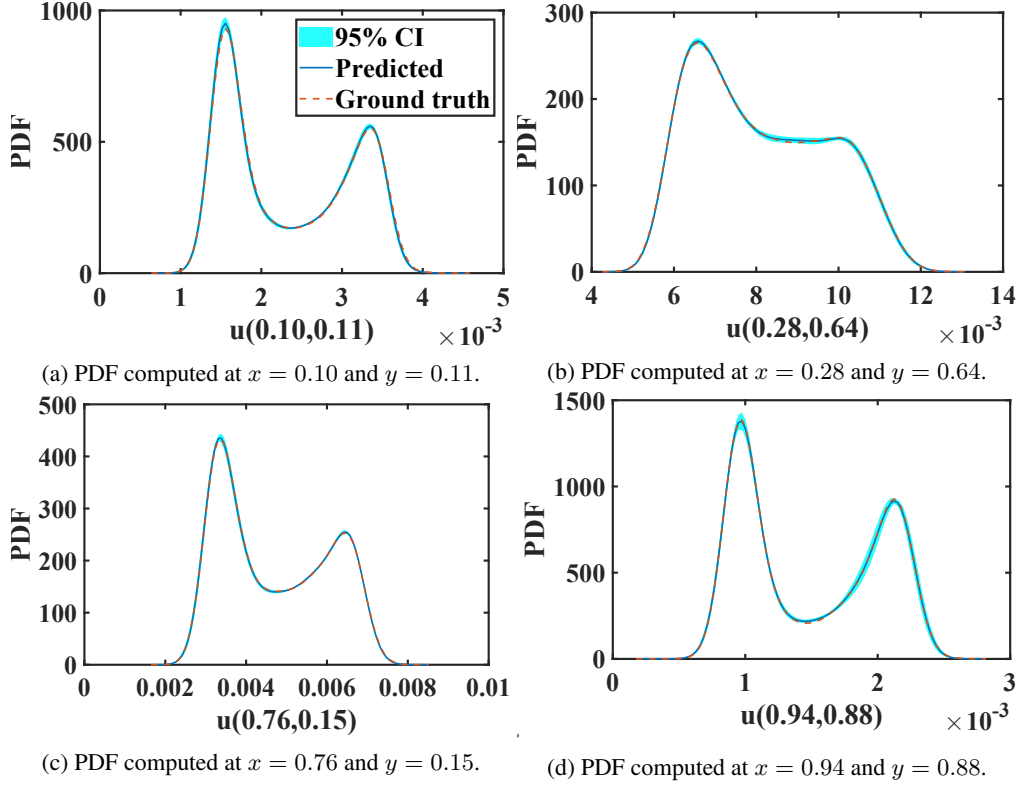


Figure 7: Aleatoric uncertainty estimated for two-dimensional Darcy flow in CS-II.

equation is not solved directly, but instead, the two-dimensional acoustic wave equation is solved first in the time domain, and the results produced are then transferred to the frequency domain in order to obtain the pressure wavefield  $u(x, z)$ . The two-dimensional acoustic wave equation is defined as,

$$\nabla^2 p(x, z, t) - \frac{1}{v(x, z)^2} \frac{\partial^2 p(x, z, t)}{\partial t^2} = s(x_s, z_s, t), \quad (13)$$

where  $p(x, z, t)$  is the pressure wavefield in time domain and  $v(x, z)$  is the velocity of wave at location  $(x, z)$ . The point source  $s$  is located at the location  $(x_s, z_s)$ . The spatial domain  $(x, z) \in [0 \text{ m}, 690 \text{ m}]^2$  in Eq. (13) is discretized with  $\Delta x = \Delta z = 10 \text{ m}$  and a constant source of magnitude 1 is selected for modeling. The variability in different samples is introduced by virtue of changing velocity models, which are obtained from [50] (FlatVel-A dataset, Vel Family). The source location is fixed at  $x_s = 680 \text{ m}$  and  $z_s = 10 \text{ m}$ . Now, the pressure wavefield in the frequency domain can be computed for a wide range of frequencies, but the initial lower frequencies will contribute the majority of the energy. As a result, to test the efficacy of the proposed RP-WNO, the dataset created contains pressure wavefields corresponding to frequencies 1Hz, 3Hz, 5Hz, 7Hz, and 9Hz.

Now, although we can use different RP-WNO ensembles for mapping velocity field to pressure wavefield of different frequencies, to show the efficacy of the proposed operator learning framework, the mapping in the current case study is carried out for all five frequencies using a single RP-WNO ensemble. To achieve this, the input to RP-WNO, which was supposed to be the velocity field and the grid on which it is discretized, is concatenated with an additional matrix that contains the frequency information corresponding to which output is obtained. The additional matrix being concatenated has the same dimensions as the velocity wavefield, and its elements have a constant value equal to the frequency under consideration. For example, if corresponding to velocity field  $v(x, z) = \mathbf{V}_1$ , we have pressure wavefield  $u(x, z; w) = \mathbf{U}_1^{(w)}$ , we will obtain five samples for training the proposed RP-WNO, which can be visualized

as follows,

Inputs	Outputs	
$\mathbf{V}_1, 1\mathcal{U}, \mathcal{G}_x, \mathcal{G}_z$	$\mathbf{U}_1^{(1)}$	
$\mathbf{V}_1, 3\mathcal{U}, \mathcal{G}_x, \mathcal{G}_z$	$\mathbf{U}_1^{(3)}$	
$\mathbf{V}_1, 5\mathcal{U}, \mathcal{G}_x, \mathcal{G}_z$	$\mathbf{U}_1^{(5)}$	
$\mathbf{V}_1, 7\mathcal{U}, \mathcal{G}_x, \mathcal{G}_z$	$\mathbf{U}_1^{(7)}$	
$\mathbf{V}_1, 9\mathcal{U}, \mathcal{G}_x, \mathcal{G}_z$	$\mathbf{U}_1^{(9)}$	(14)

where  $\mathcal{U}$  is a unity matrix with the same dimensions as the matrix  $\mathbf{V}_1$ .  $\mathcal{G}_x$  and  $\mathcal{G}_z$  are the matrices containing the grid information on which  $\mathbf{V}_1$  is discretized. To train the RP-WNO ensembles, 500 velocity models are used. Additionally, the pressure wavefield in the frequency domain will be represented by complex numbers. Hence, the real and imaginary components of the pressure wavefield  $u(x, z; w)$  are trained separately using two different RP-WNO ensembles. Fig. 8 shows the mean RP-WNO predictions compared against the ground truth for the real part of the

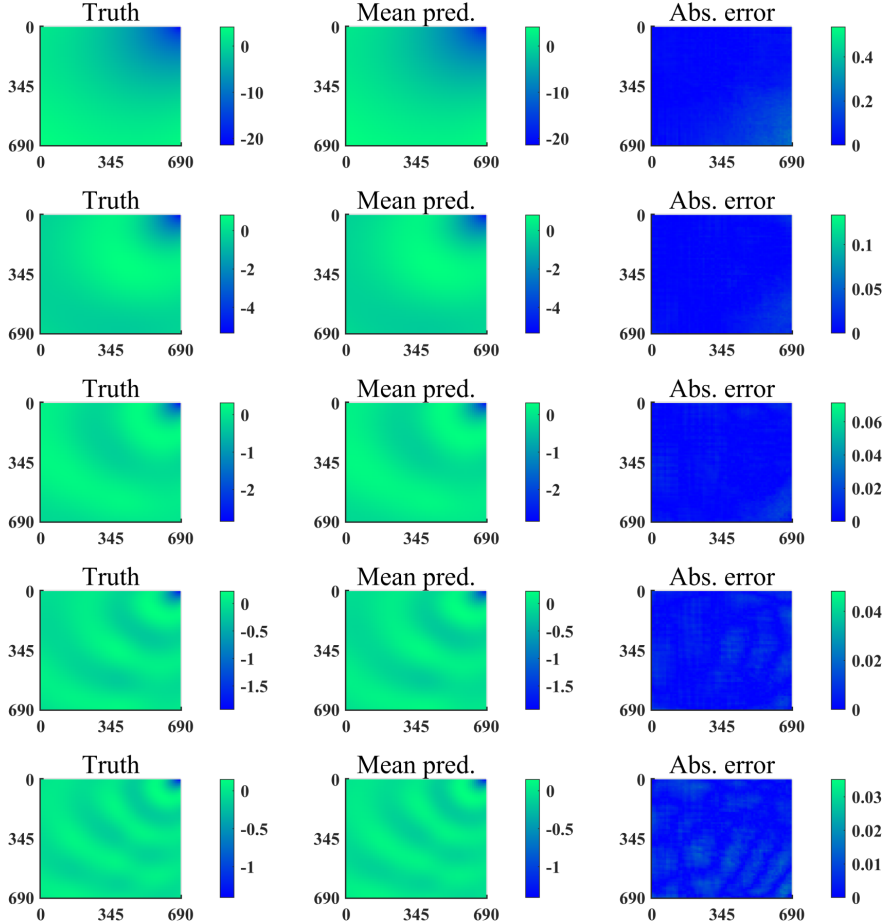


Figure 8: Pressure wavefield predictions (real part) corresponding to one sample of the velocity field, obtained using the trained RP-WNO ensemble. The result corresponding to a frequency equal to 1Hz is given at the top, and the one corresponding to 9Hz is given at the bottom. Results in between correspond to frequencies of 3Hz, 5Hz, and 7Hz, respectively, from top to bottom.

pressure wavefield. The results shown correspond to a frequency of 1Hz, 3Hz, 5Hz, 7Hz, and 9Hz, from top to bottom, and as can be seen, the mean prediction from RP-WNO closely follows the ground truth.

Figs. 9 and 10 show the aleatoric uncertainty estimates for the real part of the pressure wavefield corresponding to different frequencies. Five thousand different velocity models were used in order to obtain the stipulated results. Part (a) of Figs. 9 and 10 show results corresponding to RP-WNO ensemble utilizing discrete wavelet transform. In this, among the four wavelet coefficients of the discrete wavelet transform, only the approximate and the horizontal components are learned while training. Although the mean predictions for the RP-WNO model trained using discrete

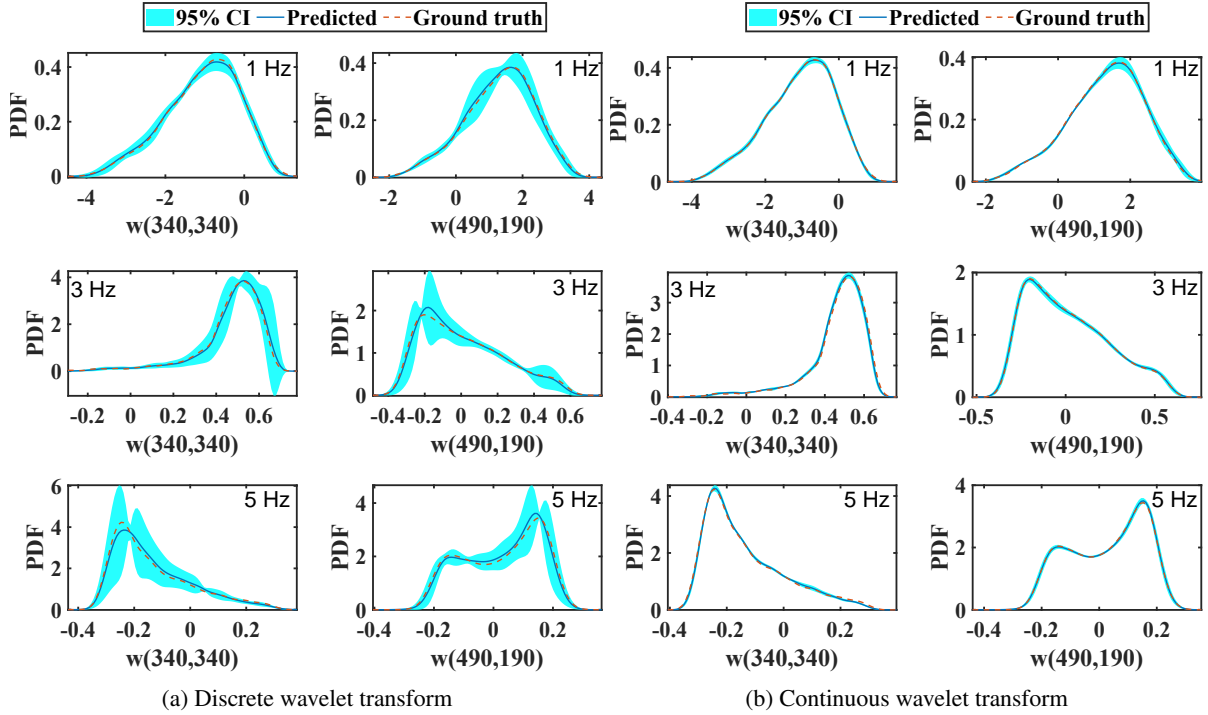


Figure 9: Alleatoric uncertainty estimates for the Pressure wavefield (real part), computed corresponding to different frequencies (1Hz, 3Hz, and 5Hz). PDFs are computed at two locations, (i)  $x = 340, z = 340$  and (ii)  $x = 490, z = 190$ .

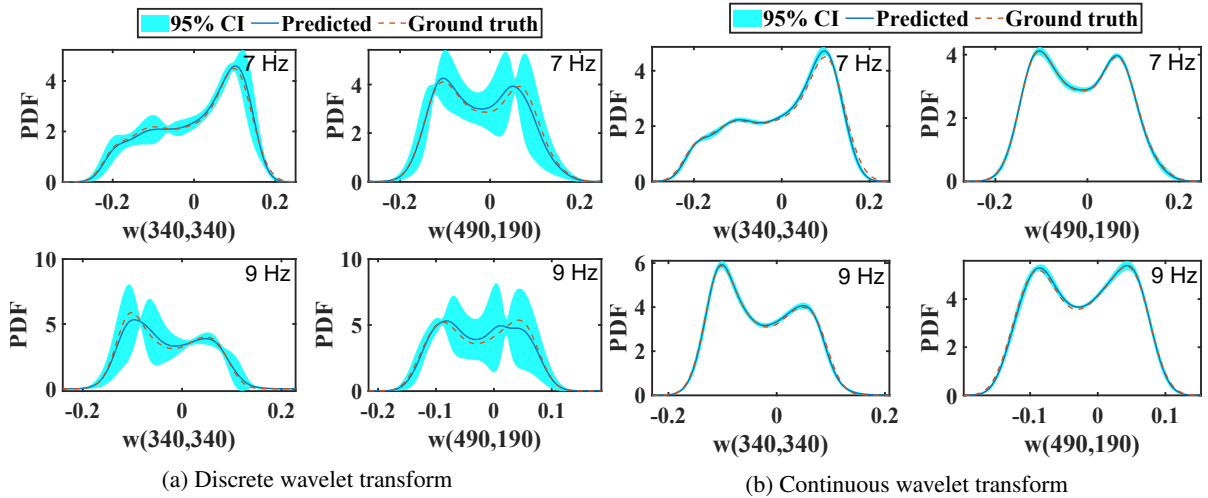


Figure 10: Alleatoric uncertainty estimates for the Pressure wavefield (real part), computed corresponding to different frequencies (7Hz and 9Hz). PDFs are computed at two locations, (i)  $x = 340, z = 340$  and (ii)  $x = 490, z = 190$ .

wavelet transform, give a reasonable approximation of the ground truth, the uncertainty observed in predictions is huge owing to the slight deviations observed in the prediction results.

On the other hand, part (b) of Figs. 9 and 10 show the predictions of the RP-WNO ensemble utilizing continuous wavelet transform. In this, all the wavelet coefficients of the continuous wavelet transform were learned, and as can be seen that the mean predictions in this case closely follow the ground truth, and correspondingly tight uncertainty bounds are obtained for the predicted results.

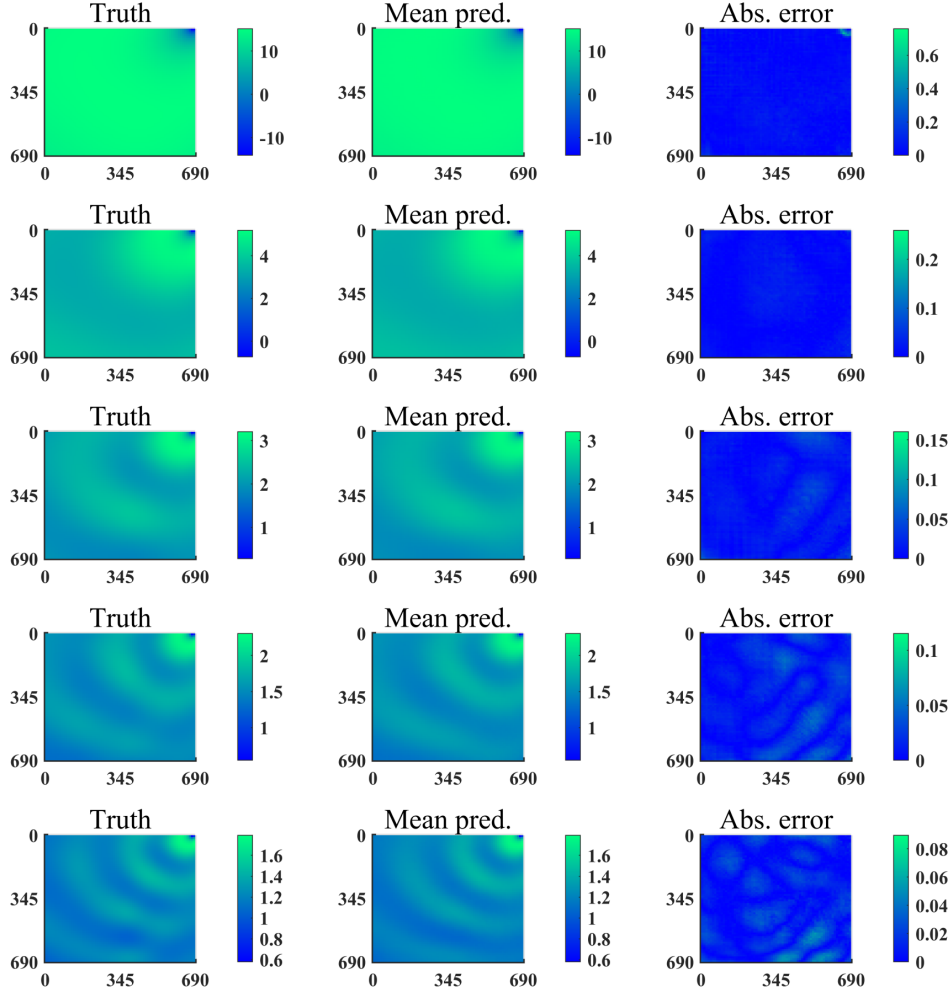


Figure 11: Pressure wavefield predictions (imaginary part) corresponding to one sample of the velocity field, obtained using the trained RP-WNO ensemble. The result corresponding to a frequency equal to 1Hz is given at the top, and the one corresponding to 9Hz is given at the bottom. Results in between correspond to frequencies of 3Hz, 5Hz, and 7Hz, respectively, from top to bottom.

Fig. 11 shows the mean RP-WNO predictions compared against the ground truth for the imaginary part of the pressure wavefield. The results shown correspond to a frequency of 1Hz, 3Hz, 5Hz, 7Hz, and 9Hz, from top to bottom, and as can be seen, the mean prediction obtained from the trained RP-WNO ensemble, closely follows the ground truth.

Figs. 12 and 13 show the aleatoric uncertainty estimates for the real part of pressure wavefield corresponding to different frequencies. Five thousand different velocity models were used in order to obtain the stipulated results. The predictions are obtained using the RP-WNO model utilizing continuous wavelet transform. All the wavelet coefficients of the continuous wavelet transform were learned, and similar to the aleatoric uncertainty estimates of the real part, the mean predictions closely follow the ground truth giving a tight associated uncertainty bound.

### 3.4 CS-IV: Mesoscale properties

Having looked at some arguably conventional operator learning problems, the fourth case study will look to map the atomic structural defects to the mesoscale properties in crystalline solids. Structural defects are unavoidable when it comes to synthesizing materials, and the same affects the material properties like conductivity, elastic modulus, etc. Estimating the material property directly based on the atomic structure is non-trivial and requires extensive simulations and experiments; hence it is worthwhile to explore the efficacy of the proposed RP-WNO in learning the mapping between the two.

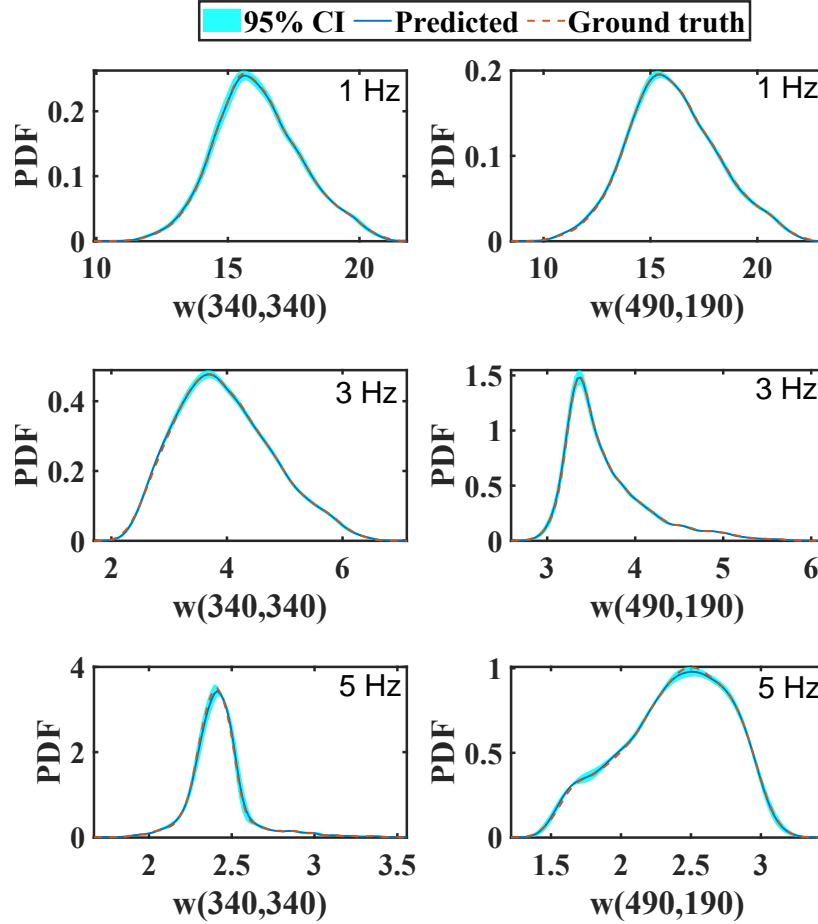


Figure 12: Alleatoric uncertainty estimates for the Pressure wavefield (imaginary part), computed corresponding to different frequencies (1Hz, 3Hz, and 5Hz).

In this case study, the mapping is carried out between the initial atomic structure of a two-dimensional porous graphene sheet of size  $127.9\text{\AA} \times 127.8\text{\AA}$  and the atomic stresses corresponding to a tensile strain of 5%. Different samples are generated by varying the location of vacancies in the porous graphene sheet randomly. The dataset for this case study is taken from [51], and the readers are advised to follow the same for more details regarding the dataset generation.

Fig. 14 shows the RP-WNO predictions compared against the ground truth. The RP-WNO ensemble was trained using 1500 training samples, and the mean predictions closely follow the ground truth. Fig. 15 shows the confidence intervals and mean predictions corresponding to one sample of the prediction ensemble. As can be seen that the mean predictions largely give a good approximation for the ground truth, and for cases where some deviation is observed, the ground truth is almost always encapsulated by the confidence intervals.

CS-I	CS-II	CS-III					CS-IV	
		frequency	1Hz	3Hz	5Hz	7Hz		9Hz
0.080	0.095	real part	0.082	0.100	0.250	0.674	1.918	2.527
		imaginary part	0.002	0.003	0.005	0.008	0.013	

Table 3: Percentage NMSE error values for various case studies.

Percentage normalized mean square error values for various case studies are given in Table 3.

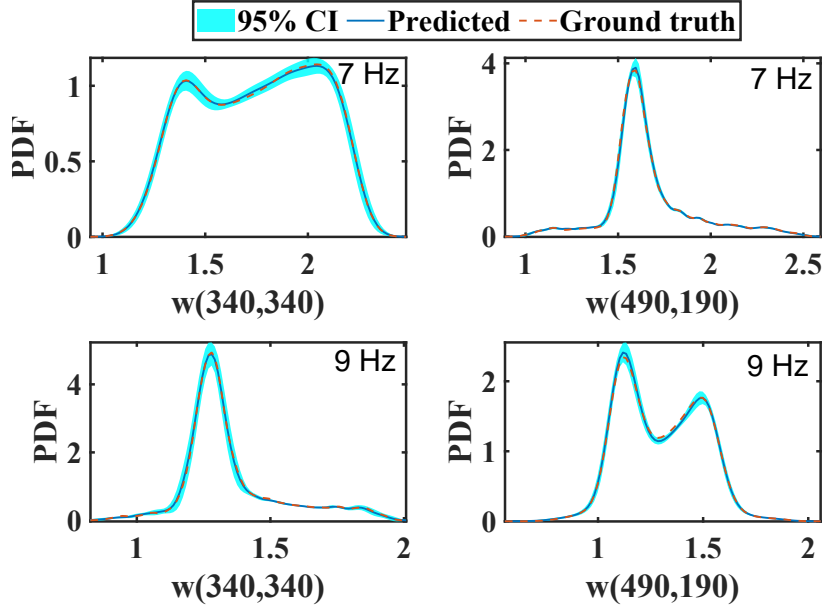


Figure 13: Alleatoric uncertainty estimates for the Pressure wavefield (imaginary part), computed corresponding to different frequencies (7Hz and 9Hz).

## 4 Conclusion

In this paper, we introduce a novel randomized prior wavelet neural operator, which is an operator learning framework and is capable of estimating the uncertainty associated with its predictions. Although Bayesian inference based techniques are often cited when it comes to uncertainty quantification, their complexity and heavy resource requirement can cause hindrances in their augmentation with complex deep learning architectures. The proposed algorithm gains an advantage here as it is set in the deterministic framework and hence can be trivially implemented for complex deep neural network architectures. The proposed RP-WNO is based on WNO, which utilizes wavelet transform and convolutional layers in order to learn the most relevant information and keep the parameter requirement relatively low for the overall network.

The proposed RP-WNO is trained in an ensemble training setup, which enables uncertainty quantification in the prediction stage. Its advantage over vanilla ensemble training is that by virtue of randomized prior networks, it can encode prior information while training. Uncertainty quantification in the prediction stage can be instrumental for applications where decision-making is involved, and an efficient operator learning framework can by itself be used as a surrogate model in a vast array of applications. To test the proposed framework, four different case studies have been carried out, and the predicted results are compared against the ground truth. The following observations have been made based on the results produced,

- The mean predictions in all case studies closely follow the ground truth and give a good approximation for the same.
- The training data case studies carried out in CS-I and CS-II show that the width of the confidence intervals obtained using the proposed RP-WNO decrease as the training data is increased and as the mean prediction converges to the ground truth. This is an expected behavior and showcases the ability of the proposed RP-WNO to estimate the true uncertainty associated with its predictions.
- The comparison between prediction results obtained from the RP-WNO ensemble utilizing discrete WTs and continuous WTs, in CS-III, shows that even though continuous WT is more resource extensive, it converges better to the ground truth.
- Furthermore, while training, it was observed that when continuous WT is used within the RP-WNO architecture, the requirement for the number of nodes in the hidden layer reduces hence compensating slightly for the increased cost of performing continuous WT and learning its various wavelet coefficients.

To conclude, based on the results, it can be said that the proposed RP-WNO is able to perform its stipulated tasks efficiently and in an effective manner. Having said all this, the authors note that, like any other research, there is

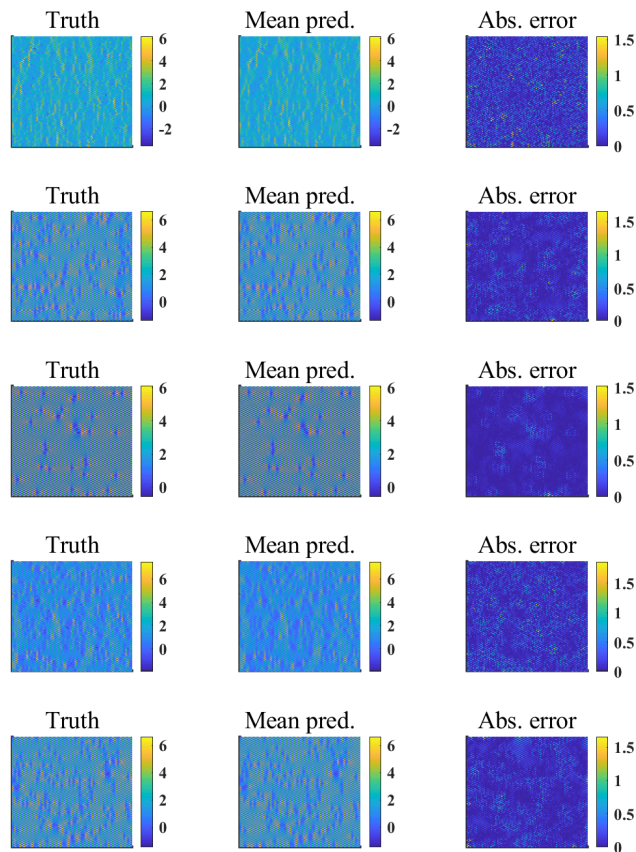


Figure 14: RP-WNO predictions compared against the ground truth for cases study IV.

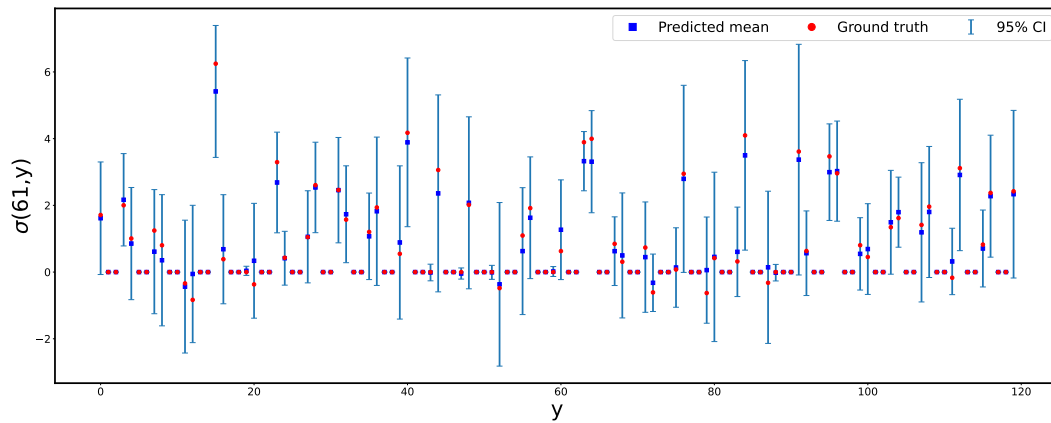
scope for improvement in the proposed RP-WNO framework. For example, research can be carried out to bring down the computational cost associated with training the RP-WNO ensemble. Also, currently, the nature of prior being introduced is not very modular as the architecture for the fixed weights network is kept the same as the trainable network. Hence, the effects of modifying the fixed weight network can be explored in future research.

## Acknowledgment

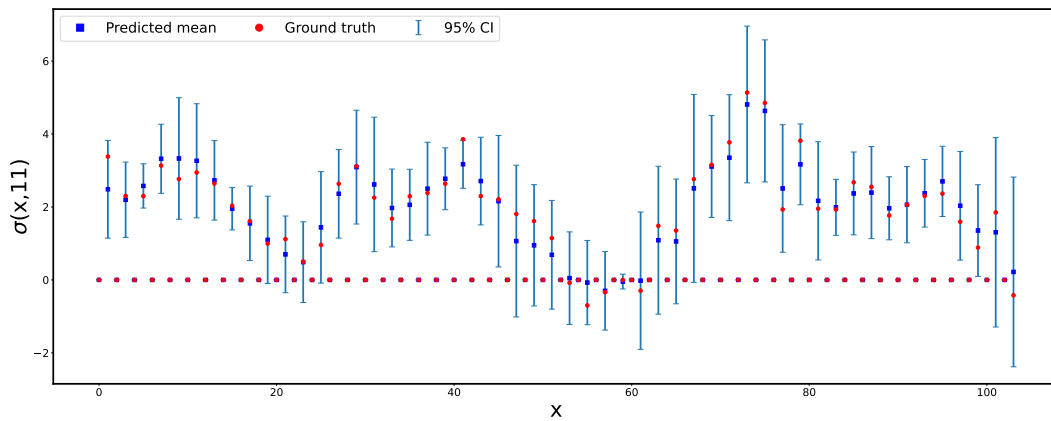
SG acknowledges the financial support received from the Ministry of Education, India, in the form of the Prime Minister’s Research Fellows (PMRF) scholarship. SC acknowledges the financial support received from Science and Engineering Research Board (SERB) via grant no. SRG/2021/000467. The authors would also like to acknowledge Tapas Tripura, Ph.D. scholar at Applied Mechanics Department, IIT Delhi, for his inputs regarding the continuous wavelet transform in wavelet neural operator.

## References

- [1] Julia Slingo and Tim Palmer. Uncertainty in weather and climate prediction. *Philosophical Transactions of the Royal Society A: Mathematical, Physical and Engineering Sciences*, 369(1956):4751–4767, 2011.
- [2] TN Palmer, GJ Shutts, R Hagedorn, FJ Doblas-Reyes, Thomas Jung, and M Leutbecher. Representing model uncertainty in weather and climate prediction. *Annual Review of Earth and Planetary Sciences*, 33(1):163–193,



(a)



(b)

Figure 15: Plots showcasing the mean prediction and the confidence intervals for one specific initial atomic structure.

2005.

- [3] FL Moon and AE Aktan. Impacts of epistemic (bias) uncertainty on structural identification of constructed (civil) systems. *Shock and Vibration Digest*, 38(5):399–422, 2006.
- [4] Brian R Mace, Keith Worden, and Graeme Manson. Uncertainty in structural dynamics. *Journal of Sound and Vibration*, 288(3):423–429, 2005.
- [5] Behnam Vakhshouri and Shami Nejadi. Limitations and uncertainties in the long-term deflection calculation of concrete structures. In *Vulnerability, uncertainty, and risk: Quantification, mitigation, and management*, pages 535–546. 2014.
- [6] Armen Der Kiureghian and Ove Ditlevsen. Aleatory or epistemic? does it matter? *Structural safety*, 31(2):105–112, 2009.
- [7] William D Rowe. Understanding uncertainty. *Risk analysis*, 14(5):743–750, 1994.
- [8] Rüdiger Rackwitz. Reliability analysis—a review and some perspectives. *Structural safety*, 23(4):365–395, 2001.
- [9] Shailesh Garg, Harshit Gupta, and Souvik Chakraborty. Assessment of deeponnet for time dependent reliability analysis of dynamical systems subjected to stochastic loading. *Engineering Structures*, 270:114811, 2022.
- [10] Souvik Chakraborty and Rajib Chowdhury. A semi-analytical framework for structural reliability analysis. *Computer Methods in Applied Mechanics and Engineering*, 289:475–497, 2015.
- [11] R Venkata Rao and Vimal J Savsani. Mechanical design optimization using advanced optimization techniques. 2012.
- [12] Tanmoy Chatterjee, Souvik Chakraborty, and Rajib Chowdhury. A critical review of surrogate assisted robust design optimization. *Archives of Computational Methods in Engineering*, 26(1):245–274, 2019.



- [13] Souvik Chakraborty, Tanmoy Chatterjee, Rajib Chowdhury, and Sondipon Adhikari. A surrogate based multi-fidelity approach for robust design optimization. *Applied Mathematical Modelling*, 47:726–744, 2017.
- [14] Pierrick Kersaudy, Bruno Sudret, Nadège Varsier, Odile Picon, and Joe Wiart. A new surrogate modeling technique combining kriging and polynomial chaos expansions—application to uncertainty analysis in computational dosimetry. *Journal of Computational Physics*, 286:103–117, 2015.
- [15] Lukas Novak and Drahomir Novak. Polynomial chaos expansion for surrogate modelling: Theory and software. *Beton-und Stahlbetonbau*, 113:27–32, 2018.
- [16] Bruno Sudret. Polynomial chaos expansions and stochastic finite element methods. *Risk and reliability in geotechnical engineering*, pages 265–300, 2014.
- [17] Dequan Zhang, Xu Han, Chao Jiang, Jie Liu, and Qing Li. Time-dependent reliability analysis through response surface method. *Journal of Mechanical Design*, 139(4):041404, 2017.
- [18] Cheng Lu, Yun-Wen Feng, Rhea P Liem, and Cheng-Wei Fei. Improved kriging with extremum response surface method for structural dynamic reliability and sensitivity analyses. *Aerospace Science and Technology*, 76:164–175, 2018.
- [19] Christian Gogu and Jean-Charles Passieux. Efficient surrogate construction by combining response surface methodology and reduced order modeling. *Structural and Multidisciplinary Optimization*, 47(6):821–837, 2013.
- [20] Subrata Chakraborty and Arunabh Sen. Adaptive response surface based efficient finite element model updating. *Finite Elements in Analysis and Design*, 80:33–40, 2014.
- [21] Umberto Alibrandi. A response surface method for stochastic dynamic analysis. *Reliability Engineering & System Safety*, 126:44–53, 2014.
- [22] Guoshao Su, Lifeng Peng, and Lihua Hu. A gaussian process-based dynamic surrogate model for complex engineering structural reliability analysis. *Structural Safety*, 68:97–109, 2017.
- [23] Bin Zhu, Tetsuya Hiraishi, Huafu Pei, and Qing Yang. Efficient reliability analysis of slopes integrating the random field method and a gaussian process regression-based surrogate model. *International Journal for Numerical and Analytical Methods in Geomechanics*, 45(4):478–501, 2021.
- [24] Souvik Chakraborty, Sondipon Adhikari, and Ranjan Ganguli. The role of surrogate models in the development of digital twins of dynamic systems. *Applied Mathematical Modelling*, 90:662–681, 2021.
- [25] Vincent Dubourg, Bruno Sudret, and Jean-Marc Bourinet. Reliability-based design optimization using kriging surrogates and subset simulation. *Structural and Multidisciplinary Optimization*, 44(5):673–690, 2011.
- [26] Yann LeCun, Yoshua Bengio, and Geoffrey Hinton. Deep learning. *nature*, 521(7553):436–444, 2015.
- [27] Li Deng, Dong Yu, et al. Deep learning: methods and applications. *Foundations and trends® in signal processing*, 7(3–4):197–387, 2014.
- [28] Pramila P Shinde and Seema Shah. A review of machine learning and deep learning applications. In *2018 Fourth international conference on computing communication control and automation (ICCCUBEA)*, pages 1–6. IEEE, 2018.
- [29] Maryam M Najafabadi, Flavio Villanustre, Taghi M Khoshgoftaar, Naeem Seliya, Randall Wald, and Edin Muharemagic. Deep learning applications and challenges in big data analytics. *Journal of big data*, 2(1):1–21, 2015.
- [30] Justin Ker, Lipo Wang, Jai Rao, and Tchoyoson Lim. Deep learning applications in medical image analysis. *Ieee Access*, 6:9375–9389, 2017.
- [31] Amir Mosavi, Mohsen Salimi, Sina Faizollahzadeh Ardabili, Timon Rabczuk, Shahaboddin Shamshirband, and Annamaria R Varkonyi-Koczy. State of the art of machine learning models in energy systems, a systematic review. *Energies*, 12(7):1301, 2019.
- [32] Sina F Ardabili, Amir Mosavi, Pedram Ghamisi, Filip Ferdinand, Annamaria R Varkonyi-Koczy, Uwe Reuter, Timon Rabczuk, and Peter M Atkinson. Covid-19 outbreak prediction with machine learning. *Algorithms*, 13(10):249, 2020.
- [33] James Daniell, Kazuma Kobayashi, Dinesh Kumar, Souvik Chakraborty, Ayodeji Alajo, Ethan Taber, Joseph Graham, and Syed Alam. Physics-informed multi-stage deep learning framework development for digital twin-centred state-based reactor power prediction. *arXiv preprint arXiv:2211.13157*, 2022.
- [34] M Rahman, Abid Khan, Sayeed Anowar, Md Al-Imran, Richa Verma, Dinesh Kumar, Kazuma Kobayashi, and Syed Alam. Leveraging industry 4.0—deep learning, surrogate model and transfer learning with uncertainty quantification incorporated into digital twin for nuclear system. *arXiv preprint arXiv:2210.00074*, 2022.

- [35] Romit Maulik, Kai Fukami, Nesar Ramachandra, Koji Fukagata, and Kunihiko Taira. Probabilistic neural networks for fluid flow surrogate modeling and data recovery. *Physical Review Fluids*, 5(10):104401, 2020.
- [36] Romit Maulik and Omer San. A neural network approach for the blind deconvolution of turbulent flows. *Journal of Fluid Mechanics*, 831:151–181, 2017.
- [37] Tapas Tripura and Souvik Chakraborty. Wavelet neural operator for solving parametric partial differential equations in computational mechanics problems. *Computer Methods in Applied Mechanics and Engineering*, 404:115783, 2023.
- [38] Akshay Thakur, Tapas Tripura, and Souvik Chakraborty. Multi-fidelity wavelet neural operator with application to uncertainty quantification. *arXiv preprint arXiv:2208.05606*, 2022.
- [39] Lu Lu, Pengzhan Jin, Guofei Pang, Zhongqiang Zhang, and George Em Karniadakis. Learning nonlinear operators via deepnet based on the universal approximation theorem of operators. *Nature Machine Intelligence*, 3(3):218–229, 2021.
- [40] Yibo Yang, Georgios Kissas, and Paris Perdikaris. Scalable uncertainty quantification for deep operator networks using randomized priors. *arXiv preprint arXiv:2203.03048*, 2022.
- [41] Zongyi Li, Nikola Kovachki, Kamyar Azizzadenesheli, Burigede Liu, Kaushik Bhattacharya, Andrew Stuart, and Anima Anandkumar. Fourier neural operator for parametric partial differential equations. *arXiv preprint arXiv:2010.08895*, 2020.
- [42] Maziar Raissi, Paris Perdikaris, and George E Karniadakis. Physics-informed neural networks: A deep learning framework for solving forward and inverse problems involving nonlinear partial differential equations. *Journal of Computational physics*, 378:686–707, 2019.
- [43] George EP Box and George C Tiao. *Bayesian inference in statistical analysis*. John Wiley & Sons, 2011.
- [44] Dong-xiao Niu, Hui-feng Shi, and Desheng Dash Wu. Short-term load forecasting using bayesian neural networks learned by hybrid monte carlo algorithm. *Applied Soft Computing*, 12(6):1822–1827, 2012.
- [45] Theodore Papamarkou, Jacob Hinkle, M Todd Young, and David Womble. Challenges in markov chain monte carlo for bayesian neural networks. *Statistical Science*, 37(3):425–442, 2022.
- [46] Alex Graves. Practical variational inference for neural networks. *Advances in neural information processing systems*, 24, 2011.
- [47] Charles Blundell, Julien Cornebise, Koray Kavukcuoglu, and Daan Wierstra. Weight uncertainty in neural network. In *International conference on machine learning*, pages 1613–1622. PMLR, 2015.
- [48] Rahul Rahaman et al. Uncertainty quantification and deep ensembles. *Advances in Neural Information Processing Systems*, 34:20063–20075, 2021.
- [49] Ian Osband, John Aslanides, and Albin Cassirer. Randomized prior functions for deep reinforcement learning. *Advances in Neural Information Processing Systems*, 31, 2018.
- [50] Chengyuan Deng, Shihang Feng, Hanchen Wang, Xitong Zhang, Peng Jin, Yinan Feng, Qili Zeng, Yinpeng Chen, and Youzuo Lin. OpenFWI: large-scale multi-structural benchmark datasets for seismic full waveform inversion. *arXiv preprint arXiv:2111.02926*, 2021.
- [51] Zhenze Yang and Markus J Buehler. Linking atomic structural defects to mesoscale properties in crystalline solids using graph neural networks. *npj Computational Materials*, 8(1):1–13, 2022.
- [52] Dan Hendrycks and Kevin Gimpel. Gaussian error linear units (gelus). *arXiv preprint arXiv:1606.08415*, 2016.
- [53] Ingrid Daubechies. *Ten lectures on wavelets*. SIAM, 1992.

## A $\beta$ studies

The randomized prior networks require the summation of outputs from the trainable and the non-trainable networks to obtain the final output, using which backpropagation will be carried out for the trainable network. However, before adding the output from the non-trainable network, it is scaled by a factor  $\beta$ , which is user-defined and can affect the final results produced. In the available literature, [49], a  $\beta$  value of unity is suggested as optimum. To gauge the effect of  $\beta$ , when randomized prior networks are used in conjunction with WNO,  $\beta$  studies are carried out.

The RP-WNO ensemble is trained for the two-dimensional darcy flow equation from CS-II, and 100 samples were taken for training. Multiple RP-WNO ensembles are trained corresponding to different values of  $\beta$  parameter, and testing loss corresponding to each ensemble is computed.

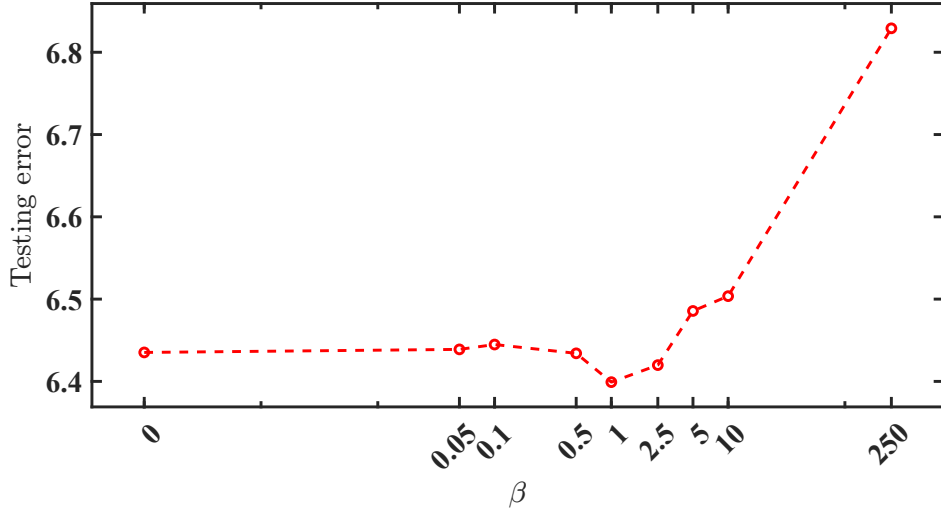


Figure 16: Effect of  $\beta$  in the RP-WNO ensemble on the testing loss.

Results shown in Fig. 16 show that a very high value of  $\beta$  adversely affects the performance of the RP-WNO ensemble. Furthermore, a very small value of  $\beta$  will reduce the effect of randomized prior, thus defeating the purpose of using a randomized prior network. It can be observed from Fig. 16 that the loss stays within a reasonable range for  $\beta = 1$ , thus reinforcing the findings from the available literature. Authors note that the additional dip in testing error observed near  $\beta = 1$  can be chalked up to a statistical anomaly, which may reduce slightly, by changing the random seed used while programming.

## B RP-WNO architecture details

Architecture details for the RP-WNO ensemble and RP-WNO models will be discussed in this section. 10 copies of RP-WNO models were used for training the RP-WNO ensembles in various case studies. Gaussian error linear unit [52] was used as activation function, and relative  $\mathcal{L}_2$  error as used in [37] is used for training the RP-WNO networks. Details for RP-WNO architectures used in various case studies are as follows.

### B.1 Architecture details CS-I

The architecture discussed below is for the trainable net, and the same is implemented for the non-trainable net. The WMC of the WNO blocks used in the trainable RP-WNO model of CS-I utilizes discrete WT (Daubechies wavelet [53]) and performs eight wavelet transforms to distill the relevant information. The wavelet coefficients obtained after the final WT are learned using the linear dense layers. Coefficients obtained in the previous WTs are used as is while inverse WT. Furthermore, inside the CMC of WNO blocks, a single convolution layer is used with a kernel size of one, to learn the inputs of CMC. Four such WNO blocks are used in the trainable RP-WNO model.

Now, the first dense layer used to uplift the trainable RP-WNO input has 64 nodes. The final forward neural net after the fourth WNO block has two dense layers with 128 nodes in the first layer and a single node in the last output layer. GeLU activation is used after the first, second, and third wavelet block and between the two dense layers of the forward neural net at the end.

### B.2 Architecture details CS-II

Similar to CS-I, WMC in CS-II utilizes discrete WT (Daubechies wavelet) and performs four WTs to distill the relevant information. The approximate and horizontal wavelet coefficients obtained after the final WT are learned using the linear dense layers. Coefficients obtained in the previous WTs and the ones which are not learned are used as is while inverse WT. Similar to architecture in CS-I, CMC of WNO blocks use a single convolution layer with a kernel size of one, to learn its inputs. Four such WNO blocks are used in the trainable RP-WNO model.

The first dense layer used to uplift the trainable RP-WNO input has 64 nodes, and the final forward neural net has two dense layers with 192 nodes in the first layer and a single node in the last output layer. GeLU activation is used after the first, second, and third wavelet block and between the two dense layers of the forward neural net at the end.

### B.3 Architecture details CS-III

WMC in CS-III utilizes continuous WT and performs four WTs to distill the relevant information. All wavelet coefficients obtained after the final WT are learned using the linear dense layers. Coefficients obtained in the previous WTs are used as is while inverse WT. Similar to previous architectures, the CMC of WNO blocks uses a single convolution layer with a kernel size of one, to learn its inputs. Four such WNO blocks are used in the trainable RP-WNO model.

The first dense layer used to uplift the trainable RP-WNO input in CS-III has 64 nodes, and the final forward neural net has two dense layers with 64 nodes in the first layer and a single node in the last output layer. GeLU activation is used after the first, second, and third wavelet block and between the two dense layers of the forward neural net at the end. The architecture used to train the RP-WNO ensemble learning the real part of the pressure wavefield is kept the same as the one used for learning the imaginary part of the pressure wavefield.

### B.4 Architecture details CS-IV

WMC in CS-IV utilizes continuous WT as in CS-III and performs three WTs to distill the relevant information. All wavelet coefficients obtained after the final WT are learned using the linear dense layers. Coefficients obtained in the previous WTs are used as is while inverse WT. Similar to previous architectures, the CMC of WNO blocks uses a single convolution layer with a kernel size of one, to learn its inputs. Five such WNO blocks are used in the trainable RP-WNO model.

The first dense layer used to uplift the trainable RP-WNO input has 128 nodes, and the final forward neural net has two dense layers with 192 nodes in the first layer and a single node in the last output layer. GeLU activation is used after the first, second, third, and fourth wavelet block and between the two dense layers of the forward neural net at the end.